Sn-based alloys synthesized in an ionic liquid at room temperature : Cu6Sn5 as a case study

Nadia Soulmi, Ana Gabriela Porras Gutierrez, Cecile Rizzi, Juliette Sirieix-plénet, Laurent Gaillon, Henri Groult, Anne-Laure Rollet, Evrim Umut, Danuta Kruk, Mathieu Duttine, et al.

FULL PAPER

Sn-based alloys synthesized in room temperature ionic liquid: Cu_6Sn_5 as a case study

Nadia Soulmi,[a],[b] Ana Gabriela Porras Gutierrez,[a],[b] Cécile Rizzi,[a],[b] Juliette Sirieix-Plénet,[a],[b] Laurent Gaillon,[a],[b] Henri Groult,[a],[b] Anne-Laure Rollet,[a],[b] Evrim Umut,[c],[g] Danuta Kruk,[c] Mathieu Duttine,[d] Olaf. J. Borkiewicz,[e] Oleg I. Lebedev,[f] and Damien Dambournet*[a],[b]

[a] N. Soulmi, A G Porras Gutierrez, C. Rizzi, J. Sirieix-Plénet, L. Gaillon, H. Groult, A-L Rollet, D. Dambournet
Sorbonne Université, CNRS, Physico-chimie des électrolytes et nano-systèmes interfaciaux, PHENIX, F-75005 Paris, France
E-mail: damien.dambournet@sorbonne-universite.fr
[b] N. Soulmi, A G Porras Gutierrez, C. Rizzi, J. Sirieix-Plénet, L. Gaillon, H. Groult, A-L Rollet, D. Dambournet
Réseau sur le Stockage Electrochimique de l'Energie (RS2E), FR CNRS 3459, 80039 Amiens Cedex, France
[c] E. Umut, D. Kruk
Faculty of Mathematics and Computer Science, University of Warmia and Mazury in Olsztyn, Słoneczna 54, 10710 Olsztyn, Poland
[d] M. Duttine,
CNRS, Univ Bordeaux, ICMCB, UPR 9048, F-33600 Pessac, France
[e] Olaf. J. Borkiewicz
X-ray Science Division, Advanced Photon Source, Argonne National Laboratory, Argonne, Illinois, USA
[f] Oleg I. Lebedev,
Laboratoire CRISMAT, ENSICAEN, Université de Caen, CNRS, 6 Bd Maréchal Juin, F-14050 Caen, France
[g] Dokuz Eylul University, Department of Medical Imaging Techniques, 35330, Izmir, Turkey

Supporting information for this article is given via a link at the end of the document.((Please delete this text if not appropriate))

Abstract: Sn-based alloys are increasingly investigated owing to possible electronic/structural modulations of interest for electrocatalysis and energy storage applications. Here, we report on the use of a chemical system consisting of an ionic liquid (1-ethyl-3-methylimidazolium bis(trifluoromethanesulfonyl)imide: $[EMIm^+][TFSI^-]$) and Sn-based precursor $Sn(TFSI)_2$ both featuring similar anionic groups. This strategy enabled to increase the solubility of the cationic precursor in the IL and avoid the formation of side products during the precipitation of Sn-nanoparticles formed upon reaction with a reducing agent ($NaBH_4$). Using NMR relaxometry, we further established that these nanoparticles are stabilized by specific interactions with the cationic group of the IL. Targeting the composition Cu_6Sn_5, we further demonstrated that this approach can be used to prepare Sn-based alloys which could not be prepared using conventional chloride-based precursors.

Introduction

Sn-based alloys are an interesting class of materials for applications spanning from catalysis to electrochemical energy storage. Alloying serves as a mean to tune the solid electronic properties[1] and can provide enhanced electrochemical performances in lithium cells owing to the formation of an inert matrix[2]. The precise control of the atomic structure of alloys appears, however, largely dependent on the synthesis method employed. Although ionic liquids are considered as suitable solvents to prepare unusual materials, the synthesis of binary alloys is more challenging. The resulting compound may not be alloys but core-shell like nanoparticles, fused clusters, or simply a mixture of the monometallic nanoparticles.[3] This diversity of results is due to the numerous contributing factors that are the nature of the solvent, its compatibility with the metallic precursors, the reaction kinetics and metal surface interactions with the solvent.

Literature data dealing with the synthesis of Sn-based alloys in ionic liquid solvent mostly relied on the decomposition of metallic precursors. For example, Wegner et *al* reported the synthesis of ruthenium and tin metallic alloys using 1-Ethyl-3-methylimidazolium tetrafluoroborate $[BMIm^+][BF_4^-]$, leading to the formation of Ru_2Sn alloys and a mixture of a Ru_3Sn_7 and α-Sn phase.[4] Dietrich et *al* used $PtCl_2$, $SnCl_2$ or $Sn(acac)_2$ as metallic precursors, methyltrioctylammonium bis(trifluoromethylsulfonyl)imide as the solvent and triethylborohydride as the reducing agent. Pt-Sn alloy nanoparticles were obtained without being able to strictly define the synthetized phase. According to x-ray diffraction analysis, the crystalline phase obtained were indexed with cubic metallic Pt, with diffraction peaks displaced to smaller Bragg angles, indicating the incorporation of Sn into the Pt lattice, and the possible formation of randomly alloyed nanoparticles. In addition, small SnO_2 nanoparticles in close contact with alloyed nanoparticles were observed by HRTEM.[5] This illustrates the difficulty to control the composition of the alloyed phase.

To control the chemical composition of Sn-based alloys, we proposed to use metallic precursors based on $TFSI^-$ counter ions dissolved in an $[EMIm^+][TFSI^-]$ ionic liquid. The use of common anion for both metallic precursors and the ionic liquid was shown to be an effective approach to (i) increase the solubility of cations in ILs,[6,7] especially as compared to conventionally used halide salts,[8] (ii) prevent impurities related to Cl^- anions[7] and (iii) enable the successful synthesis of nanosized metals[6,7,9,10]. We selected the tin-copper system and particularly the Cu_6Sn_5 chemical composition for its possible use as an anode for lithium-ion batteries. We compared the synthesis employing $TFSI^-$ based precursors with conventionally used chloride salts.

Results and Discussion

Synthesis of metallic Sn. The precipitation of metallic Sn synthetized using $NaBH_4$ as the reducing agent in [EMIm$^+$][TFSI$^-$] ionic liquid was investigated using two salts that are $Sn(TFSI)_2$ and $SnCl_2$. In both cases, the addition of the salt and the reducing agent dissolved in [EMIm$^+$][TFSI$^-$] results in the formation of a black precipitate. **Figure 1a** gathers the X-ray diffraction powder pattern of both samples recovered after the synthesis. As previously reported,[11] the use of $SnCl_2$ led to the formation of a phase mixture consisting in β-Sn and NaCl as an impurity. The use of $Sn(TFSI)_2$ enabled to prepare single phase of β-Sn without any traces of impurity.

We further compared the particle size and polydispersity of the two samples. $Sn(TFSI)_2$ precursor led to an average particle size ~15 nm **(Figure S1)** which is larger than that observed for $SnCl_2$ (~7 nm). This increase of the particle size is accompanied by an increase of the size polydispersity going from 29 to 35%. Such differences suggest that the nature of the cationic precursor affects the nucleation/growth mechanism of metallic Sn. This can be tentatively explained by differences in metallic salt solubility. The low solubility of $SnCl_2$ precursor might result in a continuous supply of cations promoting growth of metal particles with a smaller size and a narrower distribution.[12,13]

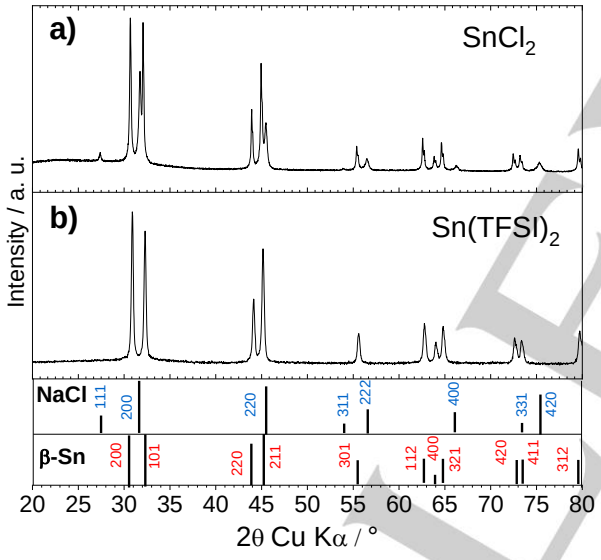

Figure 1. X-ray diffraction powder patterns of the samples prepared using a) $SnCl_2$ and b) $Sn(TFSI)_2$ as precursors.

NPs stabilization probed by NMR relaxometry. The chemical reactants used provides a versatile system to investigate the nature of the interactions between the ionic liquid and the surface of the nanoparticles. To do so, we explore the use of ^{1}H and ^{19}F spin-lattice relaxation experiments performed on a solution containing freshly precipitated β-Sn prepared using the $TFSI^-$ precursor, in the frequency range of 10 kHz – 40 MHz (referring to the ^{1}H resonance frequency).

"Classical" NMR relaxation experiments are performed at a single magnetic field while here, the magnetic field can be varied in a very broad range thanks to the concept of Fast Field Cycling[14,15], a technique well suited to probe the interactions between a solvent and nanoparticle's surfaces.[16] The great advantage of this method is its ability to probe in a single experiment, molecular and ionic dynamical processes occurring on much different time scales.[20,[19],24,25] The relaxation dispersion profiles (relaxation rates plotted versus the resonance frequency) reveal specific effects (not observed in "classical" NMR relaxation studies) that can be treated as a fingerprint of the slowing down of ionic dynamics due to interaction with surfaces. Here, we used an original approach as the experiments were performed at the frozen state and exploit the modification of the ^{14}N nuclear energy levels induced by the presence of metallic nanoparticles. Indeed, the standard approach is to record relaxation dispersion profiles in the liquid state and to model the fluctuations of the dipolar interactions – source of relaxation – experienced by the nuclei.[18],[20] In other words, the goal in liquid is to model the dynamics of the molecule: rotation, diffusion in the bulk, diffusion at the surface of the particles, etc.[18,21–25] In the present situation, it can be tricky to distinguish between the case of the cation (or anion) diffusing on the surface of the raw nanoparticles of diameter D and the case of nanoparticles covered by a layer of anion (or cation) leading to a diameter of D+d (d being approximately 20 times smaller than D). With [EMIm$^+$][TFSI$^-$], the presence of ^{14}N in both the anion and the cation can be a source of relaxation enhancement at specific frequencies provided that the dynamic is slow. This effects is referred as Quadrupole Relaxation Enhancement (QRE).[21,[29],33–35] The ^{1}H (^{19}F) spin-lattice relaxation originates from several relaxation pathways between the ^{1}H (^{19}F) nuclei and other NMR active nuclei in the neighborhood, especially ^{14}N. As the spin quantum number of ^{14}N nuclei is larger than ½ (it is 1), the nuclei experience two kinds of interactions: Zeeman interaction and quadrupole coupling, *i.e.*, a coupling with the electric field gradient tensor at its position. For slow dynamics, the energy level structure of ^{14}N is determined by a superposition of its Zeeman and quadrupole interactions. When the ^{1}H resonance frequency (the transition frequency between the ^{1}H energy levels) matches one of the ^{14}N transition frequencies, the ^{1}H polarization can be taken over by ^{14}N, as a result of the mutual magnetic dipole-dipole coupling between the participating nuclei, leading to a frequency-specific enhancement of the ^{1}H spin-lattice relaxation rate referred to as QRE; the ^{1}H spin-lattice relaxation maxima are called quadrupole peaks. The positions of the quadrupole peaks depend on the quadrupole parameters which are determined by the electric field gradient tensor at the ^{14}N position and appear when (as already pointed out) the dynamic is sufficiently slow.[15,26–28] For ^{14}N there are three quadrupole peaks at the frequencies of $3/4\,a_Q(1-\eta/3)$, $3/4\,a_Q(1+\eta/3)$ and $a_Q(\eta/2)$ where a_Q is the quadrupolar coupling constant of ^{14}N, and η the asymmetry parameter of the electric field gradient at the position of the ^{14}N nucleus. The positions of the quadrupole peaks can be treated as markers of the ^{14}N chemical environment as a_Q and η values are sensitive to the electric field gradient.

Figure 2 a and b display the ^{1}H and ^{19}F spin-lattice relaxation rate profile for [EMIm$^+$][TFSI$^-$] at frozen state (T = -40 °C) where motions are sufficiently slow to allow QRE peaks existence. At least six clear peaks (some may be overlapped) on ^{1}H profile and four peaks on ^{19}F profile are observable. The mechanism of the ^{1}H and ^{19}F NMR relaxation is the dipole-dipole interaction that decreases as r^{-3}, r being the distance between the two dipoles, *i.e.*, ^{1}H (or ^{19}F) – ^{14}N distance for the QRE peaks. To identify the origin of the QRE peaks, we used the crystalline structure of the solid [EMIm$^+$][TFSI$^-$] solved by Choudhury et *al*[30], and listed the

different inter-atomic distances between ^{14}N and $^{1}H/^{19}F$ close neighbors **(Table S1)**. On one hand, it appears that all the ^{14}N carried by both the cation and the anion, are close to ^{1}H leading to seven observable QRE peaks. On the other hand, ^{14}N are far from ^{19}F except for the ^{14}N carried by the anion[30] leading to a lower number of QRE peaks in the ^{19}F NMR relaxation profile. Furthermore, by comparing both profiles, peaks II and III seems to be related to the ^{14}N carried by the anion.

Similar experiment was then conducted on a $[EMIm^+][TFSI^-]$ solution of β-Sn freshly prepared using $TFSI^-$ precursor. **Figure 2 c and d** show the ^{1}H and ^{19}F NMR relaxation profile for a frozen (T=-40 °C) $[EMIm^+][TFSI^-]$ solution of β-Sn. The striking feature is the strong modification of the QRE peaks at high frequencies on the ^{1}H profile. Instead of the two narrow peaks at 2.7 and 3.2 MHz, appears a broad and intense feature around 4.4 MHz. On the contrary, ^{19}F profile is weakly modified by the presence of metallic nanoparticles. The ^{1}H and ^{19}F NMR relaxation results suggest that *only* the cationic groups $[EMIm^+]$ interact strongly with the surface of the nanoparticles.

Furthermore, the same experiments were conducted on oxidized Sn nanoparticles dispersion in $[EMIm^+][TFSI^-]$. In this case, both the ^{1}H and ^{19}F profiles for oxidized Sn nanoparticles dispersion are superimposed to those of neat $[EMIm^+][TFSI^-]$ **(Figure S2)**. First, this result confirms that the chemical nature of the nanoparticles - and not the possible chemical bonding with the surface - is responsible of the strong modification of ^{14}N properties. Second, it confirms that the nanoparticles are not oxidized in the ionic liquid.

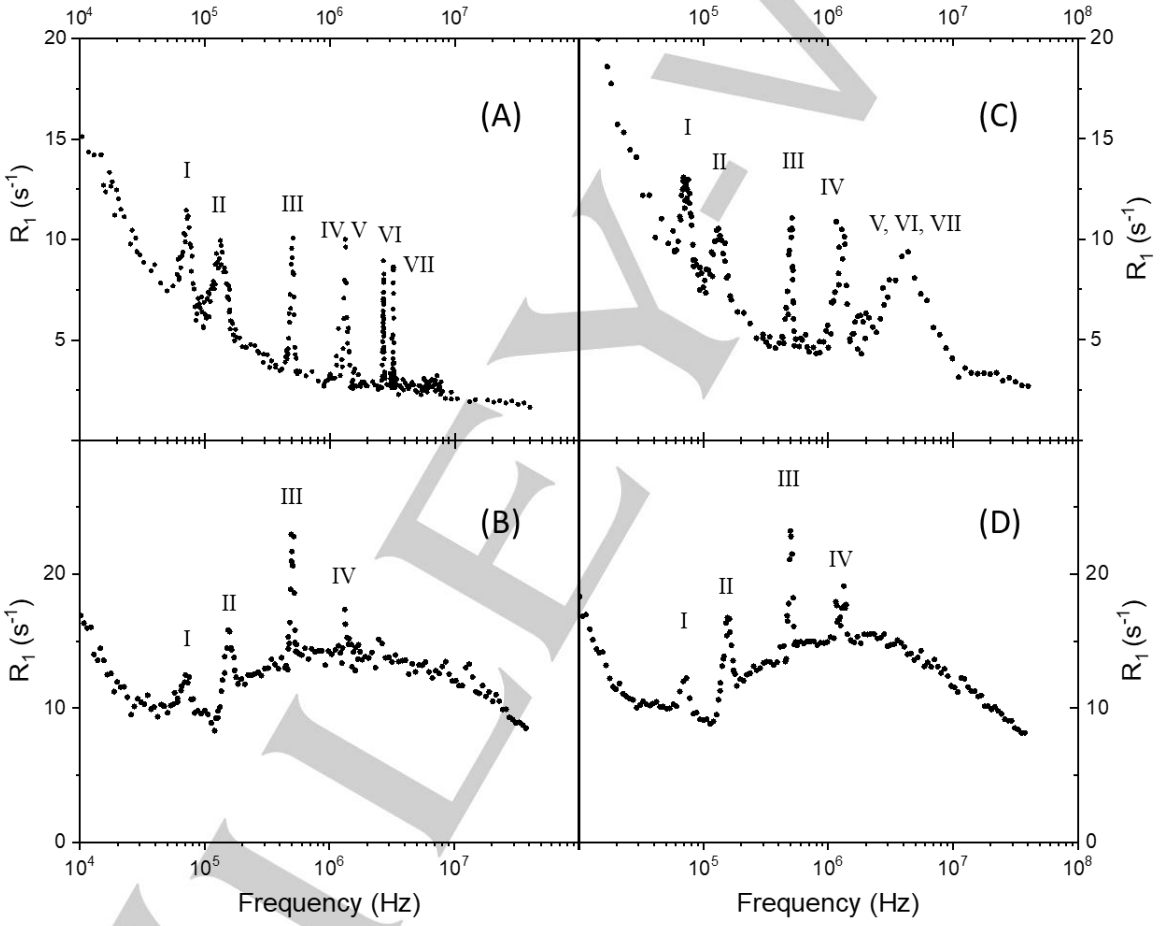

Figure 2. Spin lattice relaxation rates, R1, as a function of the frequency for frozen (A) ^{1}H and (B) ^{19}F within neat $[EMIm^+][TFSI^-]$ and (C) ^{1}H and (D) ^{19}F within β-Sn in $[EMIm^+][TFSI^-]$.

Synthesis of Cu-Sn alloys. The synthesis of Cu-Sn alloy of nominal composition Cu_6Sn_5 was first attempted using chloride precursors (see experimental section). The addition of the reducing agent led to the successive formation of a brownish precipitate followed by a black coloration **(Figure S3)**. After powder recovery, XRD analysis **(Figure 3)** revealed the formation of a phase mixture of cubic metallic Cu and β-Sn as well as NaCl as an impurity. The successive formation of monometallic nanoparticles, without the formation of Sn-Cu alloys, might be due to a concomitant effect of the low solubility of chloride precursors and standard potentials gap between Cu^{2+}/Cu (+0.34 V *vs*. SHE) and Sn^{2+}/Sn (-0.13 V *vs*. SHE).

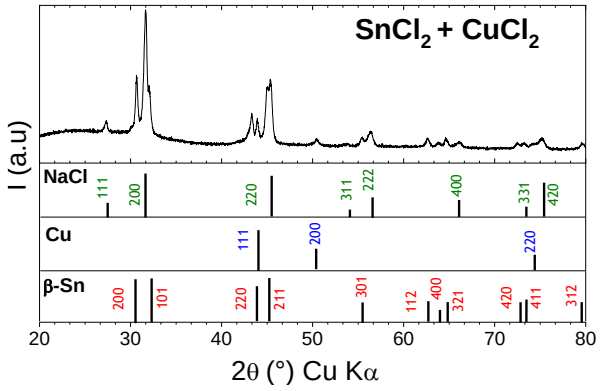

Figure 3. X-ray diffraction pattern of the sample prepared from chloride Sn-Cu precursors.

To probe the reactivity of a [EMIm$^+$][TFSI$^-$] solution containing $Sn(TFSI)_2$ and $Cu(TFSI)_2$ salts, we used cyclic voltammetry (CV) performed on an inert Mo working electrode, Pt as counter electrode and Sn as the reference. **Figure 4a** gathers the CVs of [EMIm$^+$][TFSI$^-$] solutions containing 25 mM of $Sn(TFSI)_2$ or 25 mM of $Cu(TFSI)_2$. The scan was performed at 0.05 V s^{-1} starting from the open circuit potential (E_{OCP}) toward cathodic and reversed anodic sides. Concerning the solution of Sn^{2+}, we observed a cathodic peak at -0.17 V *vs*. Sn^{2+}/Sn previously assigned to the reduction of Sn^{2+} to Sn^0 and a re-oxydation occurring at +0.10 V.[7] In the case of a 25 mM $Cu(TFSI)_2$ in [EMIm$^+$][TFSI$^-$], the voltammograms stabilized after several cycles **(Figure S4)** indicating that side reactions occurred. Thereafter, the CV showed a reduction peak at -0.02 V *vs*. Sn^{2+}/Sn, followed by an oxidation occurring at +0.53 V. Such a cathodic peak value cannot be assigned based on standard potential due to the contribution of the solvation energy of copper ions in [EMIm$^+$][TFSI$^-$] solvent.[31] Subsequently, we performed CVs on solutions of 25 mM of $Sn(TFSI)_2$ where we introduced copper with different Sn:Cu molar stoichiometries of 1.0:0.1, 1.0:0.5 and 1.0:1.2 **(Figure 4b)**.

For Sn:Cu of 1.0:0.1, the CV present a cathodic peak at -0.15 V assigned to $Sn^{2+} \rightarrow Sn^0$ and a small peak at -0.6V which might be related to Sn-Cu alloy. The anodic scan features a first intense oxidation peak at 0.02V assigned to the oxidation of Sn^0 and a small peak at 0.38V tentatively assigned to the oxidation of Sn-Cu alloy. Upon increasing the copper concentration, we did not observed cathodic peaks characteristic of the reduction of Sn^{2+} or Cu^{2+}. For Sn:Cu of 1.0:0.5, a cathodic peak is observed at -0.39V along with a broad shoulder centered at -0.77V. These two features can be assigned to the formation of Sn-Cu alloys with different Sn:Cu stoichiometries. In the anodic reverse scan, we observed three peaks at 0, 0.25 and 0.41V, assigned to the oxidation of Sn and two types of Sn-Cu alloys, respectively. For Sn:Cu of 1.0:1.2 that is the targeted nominal composition of Cu_6Sn_5, the cathodic scan displayed two broad peaks at around +0.0 and -0.6V. The anodic scan showed the absence of the peak related to Sn at 0.0V and a broad peak at +0.54V related to the formation of different Cu-Sn alloys.

Cyclic voltammetry revealed that the electrochemical responses of a solution of copper and tin in [EMIm$^+$][TFSI$^-$] depends on the Cu-Sn stoichiometry. In such a system, the measured redox potential is related to the Gibbs energy of the Sn-Cu alloy. The richness of the Sn-Cu phase diagram is reflected by the numerous peaks observed by CV. This demonstrates that the use of TFSI$^-$ precursor is a suitable approach for the control synthesis of alloys. It should be noted that attempts to measure CVs using chloride precursors failed which can be due to the low solubility of the salt.

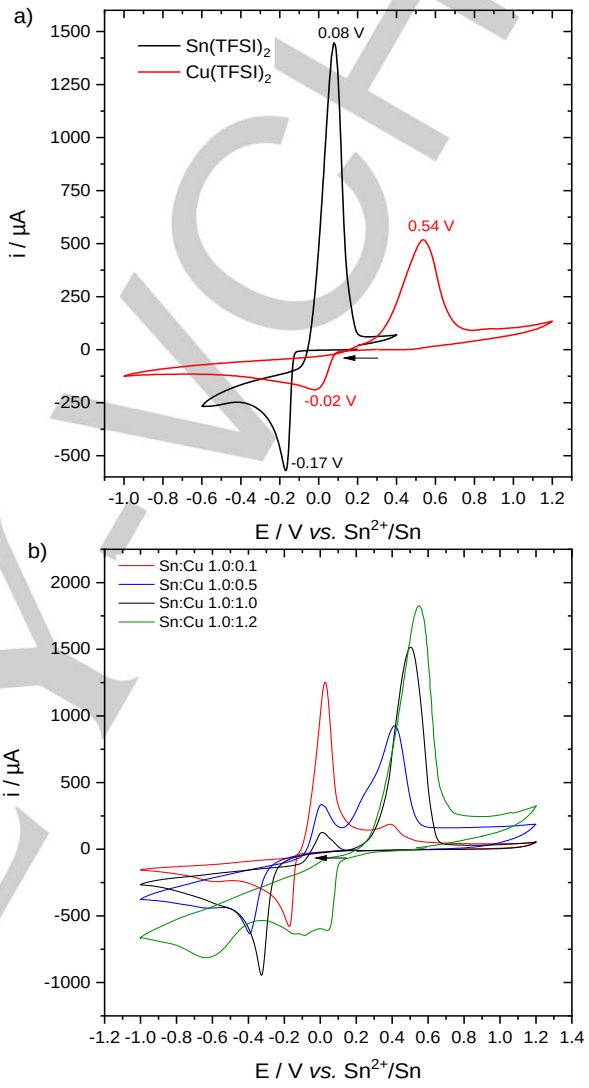

Figure 4. Cyclic voltammograms of [EMIm$^+$][TFSI$^-$] solution containing a) 25 mM $Sn(TFSI)_2$ or $Cu(TFSI)_2$ and b) 50 mM of $Sn(TFSI)_2$ and different content of $Cu(TFSI)_2$.

In agreement with cyclic voltammetry measurements, the use of TFSI-based precursors resulted in a rapid and homogeneous precipitation upon reaction with $NaBH_4$ **(Figure S3)**. The x-ray diffraction pattern measured on the recovered powder **(Figure 5)** revealed the formation of Cu-Sn based alloy without any traces of monometallic phases. TEM micrographs **(Figure S5)** showed the formation of nanoparticles with an average size of 17 nm and a large dispersity of 30 %. For the targeted composition Cu_6Sn_5, two types of polymorphs can be formed and are denoted η and η'-Cu_6Sn_5. According to the binary diagram, η'-Cu_6Sn_5 corresponds to the low-temperature phase.[32] This structure was previously solved by Larsson et *al*,[33] who described it in a monoclinic system (space group *C2/c*) presenting a NiAs-Ni_2In superstructure. The

high temperature modification η-Cu_6Sn_5 crystallizes in a hexagonal system (space group *P6₃/mmc*) and presents a NiAs-type structure.[34] Attempts to index the XRD pattern did not allow to distinct between the two η and η'-Cu_6Sn_5 polymorphs because of overlapping and broadness of the peaks.

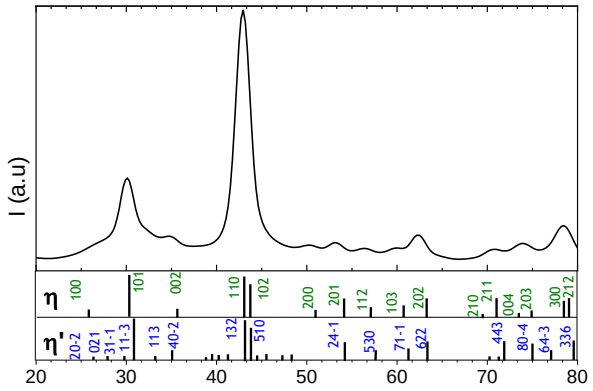

Figure 5. X-ray diffraction pattern of the sample prepared from $TFSI^-$ Sn-Cu precursors.

To study the atomic structure of the Cu-Sn alloy prepared using $TFSI^-$ based precursors, we used the pair distribution function, G(*r*), particularly suited to investigate nanostructured/disordered materials.[35] The PDF gives the interatomic distance distribution of finding atom separated from the distance *r*.[36] At the short inter-atomic distance, we noted the presence of a small peak at around 1.91 Å characteristic of Sn-O bonds indicating the presence of oxides. Attempts to refine the PDF data were performed in the *r*-range of 2.1-50 Å based on structural models of η and η'-Cu_6Sn_5 polymorphs. The quality of the refinement was quantified by the reliability factor weighted R-value, denoted R_w. The use of η-Cu_6Sn_5 as structural model fairly reproduced the PDF data with an R_w value of 29.5% **(Figure S6)**. Structural model based on η'-Cu_6Sn_5 polymorph improved the fit with an R_w value of 24.8% **(Figure S6)**. Finally, a two-phase refinement including both polymorphs as structural models led to a better fit with an R_w value of 20.7% **(Figure 6)**. The refinement of the scale factor, however, indicated that the η' polymorph was the dominant phase, *i.e.*, the mass percents of the η' and η phases were 97 and 3%, respectively. The refinement included a size parameter to account for the finite size effect of the nanoparticles on the PDF with a refined value of 11 nm which agrees with TEM observations. The structural parameters of the dominant η' phase extracted from the PDF refinement are gathered in **Table 1** and compared with literature data. Attempts to refine the rate occupancy of Sn atoms improved the fit and revealed the presence of a large content of Sn vacancies. The chemical formula determined from the refinement yielded to $Cu_6Sn_{3.3}\square_{1.7}$ where □ represents vacancy. Furthermore, the volume of the cell was slightly larger than the stoichiometric compound suggesting structural distortions which might be due to size effect and/or due to the presence of vacancies.

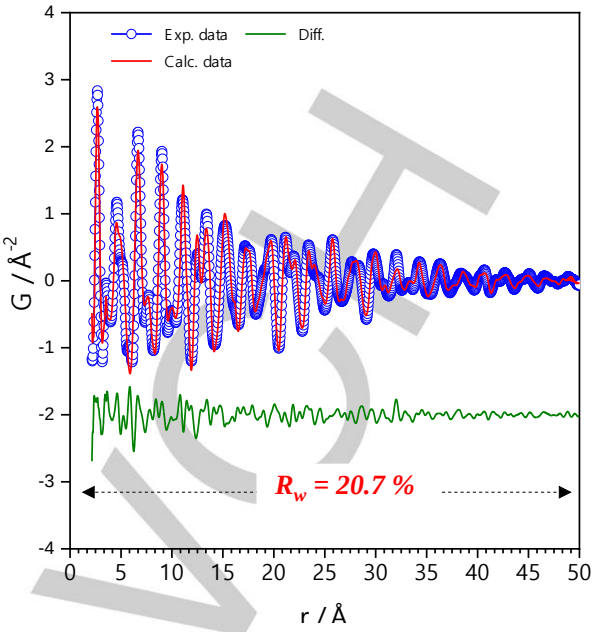

Figure 6. PDF refinement of the sample prepared from $TFSI^-$ Sn-Cu precursors.

Table 1. Structural parameters of the sample prepared from TFSI- precursors extracted from the PDF refinement. Structural parameters of the reference compound η'-Cu_6Sn_5 were added for comparison purpose.

Parameters	This work	η'-Cu_6Sn_5
Unit cell parameters		
a (Å)	11.13(2)	11.022(5)
b (Å)	7.38(1)	7.282(4)
c (Å)	9.74(2)	9.827(2)
beta	98.84	98.84
V (Å^3)	792.32	779.37
Sn atomic occupancy		
Sn(1) – 8f	0.53(8)	1.0
Sn(2) – 8f	0.75(8)	1.0
Sn(3) – 4e	0.75(9)	1.0

The chemical composition of the phase was further investigated using high-angle annular dark-field (HAADF) imaging with a scanning transmission electron microscope (STEM) coupled with Energy-dispersive X-ray (EDX) spectroscopy. **Figure 7a** shows the HAADF-STEM image of an isolated particle presenting a core-shell morphology. The observation of lattice fringes (see **Figure S7** for detailed view) in the core region suggested that it is crystallized. In contrast, the shell appeared amorphous. EDX measured on this individual particle yielded Cu_2Sn_1 composition which was close to that found by PDF refinement, *i.e.*, $Cu_2Sn_{1.1}$, therefore supporting the presence of Sn vacancies. EDX elemental mapping showed that Cu atoms were essentially present in the core region of the particle **(Figure 7b).** Moreover, we noted the presence of oxygen and tin at the shell level suggesting that the amorphous part was related to an oxide layer formed during the washing step[11].

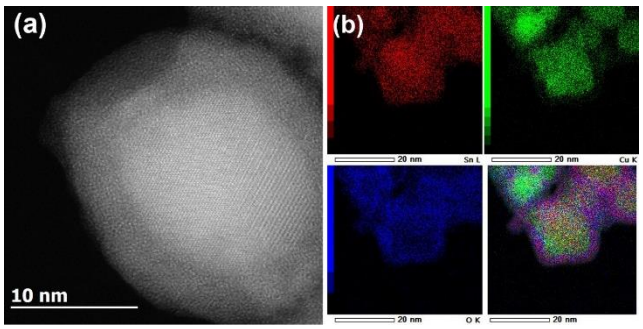

Figure 7. (a) HAADF-STEM image of an isolated particle. (b) EDX elemental mapping for Sn L, Cu K, and O K and overlay color image (right corner) on several nanoparticles. The sample was prepared from $TFSI^-$ Sn-Cu precursors.

The Mössbauer spectroscopy of ^{119}Sn (NA: 8.6%) is a powerful tool for characterizing the oxidation state and the local environment (coordination, chemical bonding, magnetic interactions, …) of tin atoms within crystalline, amorphous or intermetallic compounds. The ^{119}Sn Mössbauer spectra recorded at room temperature and 4.2 K **(Figure 8)** were reconstructed with three components corresponding to three different Sn oxidation states. These three subspectra may be associated with different Sn phases that may have different Debye temperatures and thus different Lamb-Mössbauer factors (*f*), which are related to the subspectrum absorption area. The value that the *f* factor tends towards as the temperature decreases is 1 then, at 4.2 K the subspectra relative areas **(Table 2)** correspond more accurately to the relative proportion of the three associated Sn phases. The refined Mössbauer hyperfine parameters (at 293 K) are consistent with crystalline η'-Cu_6Sn_5 for the Sn^0 quadrupole doublet with isomer shift δ = 2.09 mm.s^{-1} and a quadrupole splitting parameter (Δ) around 0.70 mm.s^{-1},[37,38] amorphous (disordered) SnO for the Sn^{2+} quadrupole doublet centered at δ = 2.96 mm.s^{-1} with a high Δ value (~1.6 mm.s^{-1})[11,39] and amorphous SnO_2 for the Sn^{4+} quadrupole doublet characterized by an isomer shift close to zero (δ = 0.06 mm.s^{-1}).[11,37] A better fit to the experimental data was achieved by considering both Sn^0 and Sn^{4+} subspectra as the weighted sum of quadrupole doublets with Lorentzian shape (line width 0.90 mm.s^{-1}) and the same isomer shift but different values of Δ, *i.e.*, with a distribution of quadrupole splitting values. The Δ distributions, which reflect some local disorder or heterogeneity in the tin electronic environment and/or the occurrence of several tin sites, are then characterized by their shape (mono- or multi-modal pattern and extent) and a mean value (labelled with the * sign in the Table 2). The Sn^0 subspectrum exhibits a bimodal distribution of the quadrupole splitting parameter with a contribution at low values (associated with symmetrical electronic environment) and a broad component centered at about 1.0 mm.s^{-1} **(Figure 8)**. This may reflect different environments for the tin nucleus depending on the distribution of tin and copper atoms in its surroundings, as expected in the η'-Cu_6Sn_5 crystalline network where three different sites have been identified for tin.[33,38] Furthermore, for copper-tin intermetallic compounds, the ^{119}Sn isomer shifts increase with the tin : metal ratio; for example, at room temperature, δ (Cu_3Sn) = 1.71 mm.s^{-1} and δ (Cu_6Sn_5) = 2.20 mm.s^{-1}.[37,38] Thus, the Sn^0 subspectrum (Figure 8) may be attributed to a tin-copper alloy with a crystalline structure similar to η'-Cu_6Sn_5 but presenting tin vacancies, as suggested by PDF refinement and EDX analysis. Hence, the ^{119}Sn Mössbauer that the Sn-Cu NPs synthesized using $TFSI^-$ precursors present a core of intermetallic tin-copper alloy (51%), and a shell containing SnO (10%) and SnO_2 (39%) at the outer surface in good agreement with the HAADF-STEM and EDS analyses.

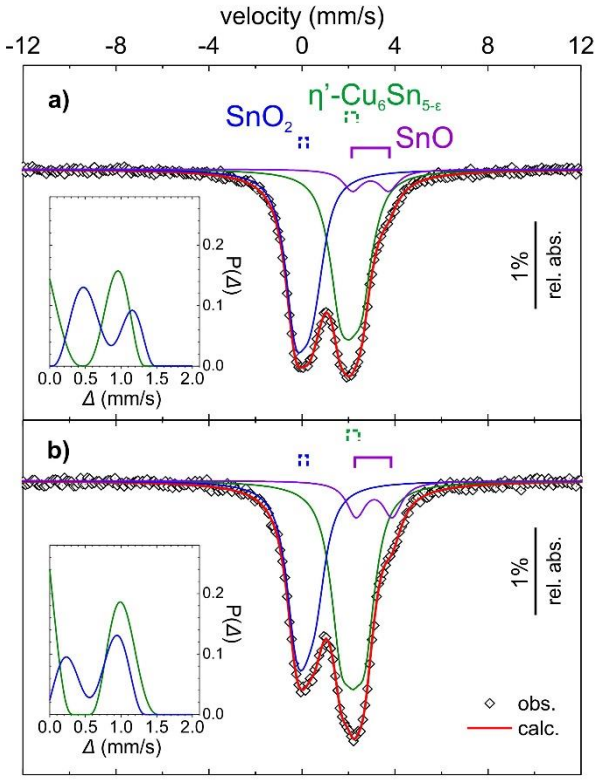

Figure 8. ^{119}Sn Mössbauer spectra recorded at room temperature (a) and 4.2 K (b) of Sn-Cu alloy synthesized with $TFSI^-$ precursors. Dots represent the observed experimental data and solid lines the calculated spectra with three distinct components associated with tin-copper intermetallic phase and tin(II) or tin(IV) oxide. Insets: distributions of the quadrupole splitting parameter.

Table 2. Refined ^{119}Sn Mössbauer hyperfine parameters of tin-copper alloy NPs synthesized in [$EMIm^+$][$TFSI^-$].

		δ (mm.s^{-1})	Δ (mm.s^{-1})	Γ (mm.s^{-1})	Rel. area (%)
293 K	η'-$Cu_6Sn_{5-x}\square_x$	2.09(2)	0.70*	0.90(-)	47(3)
	SnO	2.96(2)	1.55(5)	0.99(5)	7(3)
	SnO_2	0.06(2)	0.72*	0.90(-)	46(3)
4.2 K	η'-$Cu_6Sn_{5-x}\square_x$	2.19(2)	0.76*	0.90(-)	51(3)
	SnO	3.07(3)	1.55(5)	0.96(3)	10(3)
	SnO_2	0.11(3)	0.66*	0.90(-)	39(3)

*δ: isomer shift (rel. to $BaSnO_3$) ; Δ: quadrupole splitting ; Γ: Lorentzian linewidth ; * mean value of the quadrupole splitting distribution*

Concerning the electrochemical properties of Cu_6Sn_5, the theoretical capacity associated with lithium insertion for the stoichiometric compound is 605 mAh.g^{-1}. According to Larcher et *al*[40], the electrochemical mechanism of bulk η'-Cu_6Sn_5 proceeds via three types of lithium insertion reactions related to (i) a solid solution behavior, (ii) a partial extrusion of Cu leading to Li_2CuSn

and (iii) a complete extrusion of Cu ultimately leading to the lithium rich phase $Li_{22}Sn_5$. During the latter, Choi et *al* [41] showed that the reaction was limited to the Li_7Sn_2 composition. In bulk phases, steps (ii) and (iii) were associated to plateau region occurring at 0.4 and 0.1 V, respectively.

The electrochemical properties of $Cu_6Sn_{3.3}\square_{1.7}$ were assessed using galvanostatic discharge/charge experiments **(Figure 9a)**. The discharge/charge curves were obtained by cycling $Cu_6Sn_{3.3}\square_{1.7}$ electrode against metallic lithium under 100 $mA.g^{-1}$ within the voltage range 0.05-2.0 V. The first discharge curve featured a sloping curve with a lack of plateau region and a capacity of 1086 $mAh.g^{-1}$ largely exceeding the theoretical value. These two aspects were commonly observed for nanosized Cu_6Sn_5 with the extra capacity assigned to an irreversible conversion process of SnO_x phases.[42–45] According to the phase's proportion ($Cu_6Sn_{5-\varepsilon}$, SnO, SnO_2) determined by Mössbauer spectrometry, we calculated the theoretical capacity including the contribution of conversion and alloying reactions from SnO_x phases. This led to a value of 967 $mAh.g^{-1}$ close to that found for the first discharge **(Table S2)**. During the first charge, a capacity of 576 $mAh.g^{-1}$ was obtained. Moreover, most of this capacity was obtained within the low voltage region (<1V) which is characteristic of alloying processes, hence ruling out the contribution of conversion reactions in the overall lithiation mechanism.[46,47] Upon cycling, a stable capacity of 530 $mAh.g^{-1}$ was maintained after 90 cycles. In the used electrode formulation, a large content of carbon was added that partially contributed to the overall capacity. To account for this contribution, we subtracted it leading to a capacity close to 400 $mAh.g^{-1}$ **(Figure 9b)**. This capacity value remained, however, lower than expected for a full utilization of the Sn matrix **(Table S2)** suggesting that some Sn were inactive probably those embedded in a Li_2O matrix.

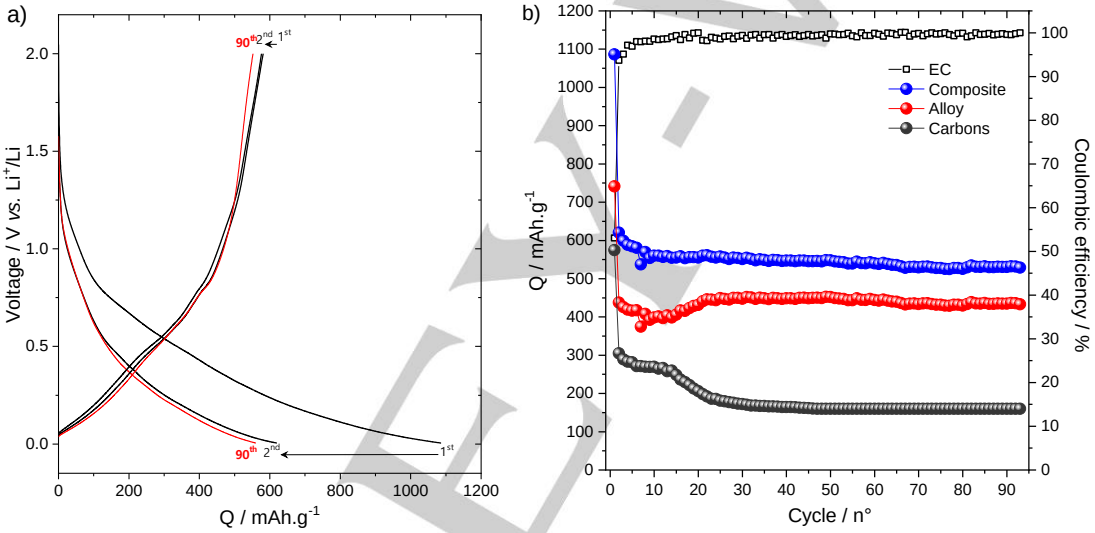

Figure 9. a) Galvanostatic discharge-charge curves of $Cu_6Sn_{3.3}\square_{1.7}$ electrode cycled *vs.* Li^+/Li. b) Evolution of the capacity as a function of cycle number for $Cu_6Sn_{3.3}\square_{1.7}$ electrode with and without the capacity contribution of carbon additive.

Conclusion

A direct synthesis of Sn and Sn-Cu alloy was developed by using metallic precursors and ionic liquid sharing the same anionic group that is $TFSI^-$. This approach enabled to avoid side impurities typically encountered using chloride precursors and allowed to stabilize alloys. NMR relaxometry of ^1H (cation) and ^{19}F (anion) further showed that NPs are surrounded by a first shell of neighbor constituted by cations of the IL. Using $TFSI^-$ precursor, we successfully prepared Sn-Cu alloy as opposed to the chloride-salt route which led to the precipitation of monometallic phases. This difference in reactivity was investigated by means of cyclic voltammetry measured on a solution containing different stoichiometries of Sn:Cu with the reduction potential (Gibbs energy) varying depending on the cation concentrations. The structure of the precipitated Sn-Cu alloy was investigated using PDF showing that it crystallized in the η' polymorph with Sn deficiency, *i.e.*, the composition determined by structural analysis was $Cu_6Sn_{3.3}\square_{1.7}$, which was further confirmed by EDX analysis. Mössbauer spectrometry allowed us to assert the occurrence of SnO_x phases located at the outer shell of the nanoparticles. The lithium insertion properties was assessed by galvanostatic cycling with a sloping voltage profile characteristic of NPs. The reversible capacity was explained by considering an alloying process. Overall, this study demonstrated that the chemical system used is an effective route for the preparation of alloys and can be certainly extended to other elements.

Experimental Section

The synthesis of Sn-based compounds was performed following a published protocol.[11,48] All operations were performed in a glove box filled with argon (H_2O and O_2 content < 1 ppm). For the synthesis of metallic Sn, a 40mM solution of $SnCl_2$ (99%, Alfa Aesar) or $Sn(TFSI)_2$ (Alfa Aesar) was prepared by dissolving the salt in 1 mL of [$EMIm^+$][$TFSI^-$] (99.5%, Solvionic). The reduction of Sn was initiated by mixing the Sn(II) solution and a 400 mM of $NaBH_4$ in 1 mL of [$EMIm^+$][$TFSI^-$] solution. For the synthesis of Cu-Sn alloy, a nominal composition of Cu_6Sn_5 was targeted. A 40 mM solution of $Sn(TFSI)_2$ and $Cu(TFSI)_2$ (Alfa Aesar) was prepared by dissolving cationic precursors in the targeted stoichiometry, in 1 mL of

[EMIm$^+$][TFSI$^-$]. After the addition of a 400 mM of $NaBH_4$ in 1 mL of [EMIm$^+$][TFSI$^-$] solution, the mixture was stirred at room temperature for six hours. The powder was separated from the IL by centrifugation and then washed with acetone and water.

X-ray diffraction pattern were measured using a Rigaku Ultima IV X-ray diffractometer with a Cu Kα radiation (λ= 1.54059 Å) with a scan rate of 0.1°min^{-1} between 10° and 80° (2θ).

The measurements of the ^{1}H and ^{19}F nuclear magnetic resonance (NMR) relaxation rates R_1=1/ T_1 have been carried out on a Stelar Spinmaster Fast Field Cycling (FFC) relaxometer. In this case, only R_1 has been measured using a pre-polarized (PP) sequence from 10 kHz to 8 MHz and a non-polarized (NP) sequence from 10 MHz to 30 MHz.[49] The parameters used for the experiments were the following: 90° RF pulse duration: 8.5 (9.5) µs, the acquisition frequency: 15.8 MHz, for ^{1}H (^{19}F) relaxation measurements. The recycle delay between two consecutive acquisitions was set to fivefold the longest spin-lattice time at the highest relaxation field, the polarization time was set to fourfold the spin–lattice time at 25 MHz (referring to the ^{1}H resonance frequency). Magnetization values were recorded for 16 logarithmically spaced values of evolution times; in the whole frequency range, the evolution of magnetization was monoexponential within experimental error. The temperature value was set at 233K and checked before and after measurements to ensure a stability of ± 0.5 K.

The high-angle annular dark field scanning transmission electron microscopy (*HAADF-STEM*) and simultaneously acquired energy-dispersive X-ray spectroscopy (EDX) elemental mapping analysis was performed on a JEM ARM200F cold FEG probe and image aberration corrected electron microscope operated at 200 kV and equipped with a large solid-angle CENTURIO EDX detector. TEM sample was prepared by crushing of material in agate mortar, dispersed in ethanol and following transferring suspension to a Ni holey carbon grid.

Cyclic voltammetry (CV) curves were recorded at 0.5 Vs^{-1} in the potential range of -0.6 and +0.4 V *vs*. Sn^{2+}/Sn. All electrochemical measurements were performed in a glove box filled with argon (H_2O and O_2 content < 1 ppm). A three-electrode electrochemical cell controlled by a potentiostat (PAR 273A) was used. Mo (A = 0.503 cm²) foils was used as working electrode. The counter electrode was a Pt wire and a Sn bar was used as reference electrode. For solutions containing tin and copper, a second compartment was used with a 10 mM solution of $Sn(TFSI)_2$ to ensure stable potential measurements.

High-energy X-ray data were collected at the 11-ID-B station at the Advanced Photon Source (Argonne National Laboratory) with an X-ray energy of 86.7 keV (λ=0.1430 Å). After corrections (background and Compton scattering), Pair Distribution Functions (PDFs), G(r) were extracted from the data using PDFgetX2 software.[50] Refinements of the PDF data were performed using PDFgui,[51] with structural models from ICSD (Inorganic crystal structure database) database.[52] Refined parameters were the instrument parameters, the lattice parameters, the atomic positions, atoms rate occupancy and the scale factor. The coherence length was refined using the spherical particle size parameter ($sp_{diameter}$). The difference between the experimental observation (data) and the calculated values (model) correspond to the difference curve, which computes the quality of the refinement defined by the weighted R-factor noted R_w. The R-value describes the difference between the experimental observation (data) and the calculated value (fit) for a single data point.

^{119}Sn Mössbauer measurements were carried out using a constant acceleration Halder-type spectrometer operating in transmission geometry with a room temperature ^{119m}Sn ($CaSnO_3$) source (370 MBq). Thin absorbers containing about 15 mg.cm^{-2} of Sn (^{119}Sn natural abundance 8.59%) were placed into a liquid helium bath cryostat. Spectra were recorded from room temperature down to 4.2 K, and the refinement of Mössbauer hyperfine parameters (δ isomer shift, Δ quadrupole splitting, Γ Lorentzian line width and relative areas) was performed using both homemade programs and the *WinNormos* software (Wissenschaftliche Elektronik GmbH).[53] The ^{119}Sn isomer shifts are referenced to $BaSnO_3$ at room temperature.

The electrochemical properties of Sn-based alloy were investigated against metallic lithium using CR2032-type coin cells. The electrode formulation, adapted from Kravchyk et *al*[54], was 30 wt.% of active material, 45wt.% of carbon (1:1 mixture of Timcal®, super C-65), and 25 wt.% of carboxymethyl cellulose CMC (Aldrich, Mw = 250 000). The electrolyte was 1 M $LiPF_6$ dissolved in a mixture of ethylene carbonate (EC) and ethyl methyl carbonate (EMC) (1:1 vol. %) with 2%wt. of fluoroethylene carbonate (FEC). The cells were assembled in a glove box filled with argon (H_2O and O_2 content < 1 ppm) with lithium metal as the anode and were cycled under 100 mA.g^{-1} in the voltage range of 2.0 – 0.05 V *vs*. Li$^+$/Li.

Acknowledgements

This article is based upon work from COST Action CA15209 EURELAX "European Network on NMR Relaxometry", supported by COST (European Cooperation in Science and Technology). Labex Michem and labex Matisse are gratefully acknowledged for the financial support. The work done at the Advanced Photon Source, an Office of Science User Facility operated for the U.S. Department of Energy (DOE) Office of Science by Argonne National Laboratory, was supported by the U.S. DOE under Contract No. DE-AC02-06CH11357. The work done at the University of Warmia and Mazury in Olsztyn was financed by National Science Centre, Poland, grant number: UMO-2017/25/B/ST5/02348.

Keywords: Sn-Cu alloys, NMR relaxometry, cyclic voltammetry, ionic liquids nanoparticles, surface interactions, lithium-ion batteries

[1] X. Zheng, Y. Ji, J. Tang, J. Wang, B. Liu, H.-G. Steinrück, K. Lim, Y. Li, M. F. Toney, K. Chan, et al., *Nature Catalysis* **2019**, *2*, 55–61.

[2] K. D. Kepler, J. T. Vaughey, M. M. Thackeray, *Journal of Power Sources* **1999**, *81–82*, 383–387.

[3] M. H. G. Prechtl, P. S. Campbell, *Nanotechnology Reviews* **2013**, *2*, 577–595.

[4] S. Wegner, M. Saito, J. Barthel, C. Janiak, *Journal of Organometallic Chemistry* **2016**, *821*, 192–196.

[5] C. Dietrich, D. Schild, W. Wang, C. Kübel, S. Behrens, *Zeitschrift für anorganische und allgemeine Chemie* **2017**, *643*, 120–129.

[6] M. Tułodziecki, J.-M. Tarascon, P. L. Taberna, C. Guéry, *Electrochimica Acta* **2014**, *134*, 55–66.

[7] N. Soulmi, A.-G. Porras-Gutierrez, N. E. Mordvinova, O. I. Lebedev, C. Rizzi, J. Sirieix-Plénet, H. Groult, D. Dambournet, L. Gaillon, *Inorg. Chem. Front.* **2019**, *6*, 248–256.

[8] B. C. M. Martindale, S. E. Ward Jones, R. G. Compton, *Physical Chemistry Chemical Physics* **2010**, *12*, 1827–1833.

[9] L. L. Lazarus, C. T. Riche, B. C. Marin, M. Gupta, N. Malmstadt, R. L. Brutchey, *ACS Appl. Mater. Interfaces* **2012**, *4*, 3077–3083.

[10] T. Liu, R. Vilar, S. Eugénio, J. Grondin, Y. Danten, *J Appl Electrochem* **2015**, *45*, 87–93.

[11] N. Soulmi, D. Dambournet, C. Rizzi, J. Sirieix-Plénet, M. Duttine, A. Wattiaux, J. Swiatowska, O. J. Borkiewicz, H. Groult, L. Gaillon, *Inorg. Chem.* **2017**, *56*, 10099–10106.

[12] J. Polte, M. Herder, R. Erler, S. Rolf, A. Fischer, C. Würth, A. F. Thünemann, R. Kraehnert, F. Emmerling, *Nanoscale* **2010**, *2*, 2463–2469.

[13] E. V. Shevchenko, D. V. Talapin, A. L. Rogach, A. Kornowski, M. Haase, H. Weller, *J. Am. Chem. Soc.* **2002**, *124*, 11480–11485.

[14] R. Kimmich, E. Anoardo, *Progress in Nuclear Magnetic Resonance Spectroscopy* **2004**, *44*, 257–320.

[15] F. Fujara, D. Kruk, A. F. Privalov, *Progress in Nuclear Magnetic Resonance Spectroscopy* **2014**, *82*, 39–69.
[16] *Field-Cycling NMR Relaxometry*, **2018**.
[17] D. Kruk, A. Herrmann, E. A. Rössler, *Progress in Nuclear Magnetic Resonance Spectroscopy* **2012**, *63*, 33–64.
[18] J.-P. Korb, *Progress in Nuclear Magnetic Resonance Spectroscopy* **2018**, *104*, 12–55.
[19] R. Kimmich, in *NMR: Tomography, Diffusometry, Relaxometry* (Ed.: R. Kimmich), Springer Berlin Heidelberg, Berlin, Heidelberg, **1997**, pp. 125–137.
[20] R. Kimmich, in *NMR: Tomography, Diffusometry, Relaxometry* (Ed.: R. Kimmich), Springer Berlin Heidelberg, Berlin, Heidelberg, **1997**, pp. 102–115.
[21] F. Martini, S. Borsacchi, M. Geppi, C. Forte, L. Calucci, *J. Phys. Chem. C* **2017**, *121*, 26851–26859.
[22] P. Levitz, M. Zinsmeister, P. Davidson, D. Constantin, O. Poncelet, *Phys. Rev. E* **2008**, *78*, 030102.
[23] T. Zavada, R. Kimmich, J. Grandjean, A. Kobelkov, *J. Chem. Phys.* **1999**, *110*, 6977–6981.
[24] P. Levitz, *Molecular Physics* **2019**, *117*, 952–959.
[25] P. E. Levitz, *Magnetic Resonance Imaging* **2003**, *21*, 177–184.
[26] F. Winter, R. Kimmich, *Biophysical Journal* **1985**, *48*, 331–335.
[27] D. Kruk, E. Umut, E. Masiewicz, C. Sampl, R. Fischer, S. Spirk, C. Goesweiner, H. Scharfetter, *Phys. Chem. Chem. Phys.* **2018**, *20*, 12710–12718.
[28] P. H. Fries, E. Belorizky, *J. Chem. Phys.* **2015**, *143*, 044202.
[29] H. I. Mäkelä, O. H. J. Gröhn, M. I. Kettunen, R. A. Kauppinen, *Biochemical and Biophysical Research Communications* **2001**, *289*, 813–818.
[30] A. R. Choudhury, N. Winterton, A. Steiner, A. I. Cooper, K. A. Johnson, *CrystEngComm* **2006**, *8*, 742–745.
[31] P. K. Nayak, L. Yang, W. Brehm, P. Adelhelm, *Angewandte Chemie International Edition* **2018**, *57*, 102–120.
[32] S. Fürtauer, D. Li, D. Cupid, H. Flandorfer, *Intermetallics* **2013**, *34*, 142–147.
[33] A.-K. Larsson, L. Stenberg, S. Lidin, *Acta Cryst B, Acta Cryst Sect B, Acta Crystallogr B, Acta Crystallogr Sect B, Acta Crystallogr Struct Sci, Acta Crystallogr Sect B Struct Sci, Acta Crystallogr B Struct Sci Cryst Eng Mater* **1994**, *50*, 636–643.
[34] A. Gangulee, G. C. Das, M. B. Bever, *MT* **1973**, *4*, 2063–2066.
[35] S. J. L. Billinge, *Physics* **2010**, *3*.
[36] T. Egami, S. J. L. Billinge, *Underneath the Bragg Peaks: Structural Analysis of Complex Materials*, Elsevier, **2003**.
[37] E. Nordstrom, S. Sharma, E. Sjostedt, L. Fransson, L. Haggstrom, L. Nordstrom, K. Edstrom, *Hyperfine Interact.* **2001**, *136*, 555–560.
[38] J. Silver, C. Mackay, J. Donaldson, *J. Mater. Sci.* **1976**, *11*, 836–842.
[39] K. F. E. Williams, C. E. Johnson, J. A. Johnson, D. Holland, M. M. Karim, *J. Phys.: Condens. Matter* **1995**, *7*, 9485–9497.
[40] D. Larcher, L. Y. Beaulieu, D. D. MacNeil, J. R. Dahn, *J. Electrochem. Soc.* **2000**, *147*, 1658–1662.
[41] W. Choi, J. Y. Lee, H. S. Lim, *Electrochemistry Communications* **2004**, *6*, 816–820.
[42] J. Wolfenstine, S. Campos, D. Foster, J. Read, W. K. Behl, *Journal of Power Sources* **2002**, *109*, 230–233.
[43] S. Liu, Q. Li, Y. Chen, F. Zhang, *Journal of Alloys and Compounds* **2009**, *478*, 694–698.
[44] W. Cui, F. Li, H. Liu, C. Wang, Y. Xia, *J. Mater. Chem.* **2009**, *19*, 7202–7207.
[45] R. Hu, G. H. Waller, Y. Wang, Y. Chen, C. Yang, W. Zhou, M. Zhu, M. Liu, *Nano Energy* **2015**, *18*, 232–244.
[46] I. A. Courtney, J. S. Tse, O. Mao, J. Hafner, J. R. Dahn, *Phys. Rev. B* **1998**, *58*, 15583–15588.
[47] X. Liu, J. Zhang, W. Si, L. Xi, S. Oswald, C. Yan, O. G. Schmidt, *Nanoscale* **2014**, *7*, 282–288.
[48] S. L. Vot, D. Dambournet, H. Groult, A. Ngo, C. Petit, C. Rizzi, C. Salzemann, J. Sirieix-Plenet, O. J. Borkiewicz, E. Raymundo-Piñero, et al., *Dalton Transactions* **2014**, *43*, 18025–18034.
[49] E. Anoardo, G. Galli, G. Ferrante, *Appl. Magn. Reson.* **2001**, *20*, 365–404.
[50] X. Qiu, J. W. Thompson, S. J. Billinge, *Journal of Applied Crystallography* **2004**, *37*, 678–678.
[51] S. Chaudhuri, P. Chupas, B. J. Morgan, P. A. Madden, C. P. Grey, *Physical Chemistry Chemical Physics* **2006**, *8*, 5045–5055.
[52] F. Karlsruhe, *URL http://icsd. fiz-karlsruhe. de. Acessed* **2014**, 12–12.
[53] R. A. Brand, *Universität Duisburg* **2008**.
[54] K. Kravchyk, L. Protesescu, M. I. Bodnarchuk, F. Krumeich, M. Yarema, M. Walter, C. Guntlin, M. V. Kovalenko, *J. Am. Chem. Soc.* **2013**, *135*, 4199–4202.

Entry for the Table of Contents

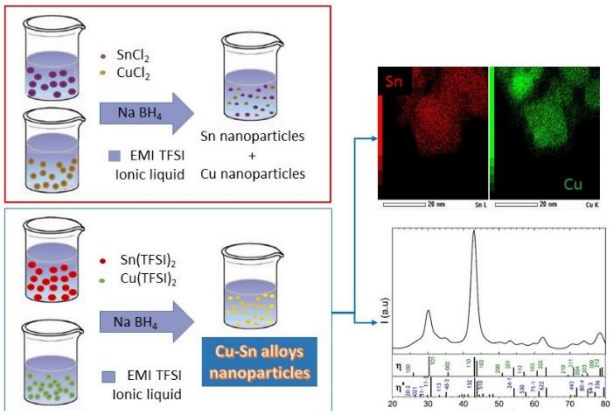

The use of a chemical system consisting of an ionic liquid (IL: [$EMIm^+$][$TFSI^-$]) and metallic precursors based on $TFSI^-$ anionic groups enabled to prepare Sn-based alloys which could not be prepared using conventional chloride precursors.